

X-Ray Emission from Supernova Remnants Observed in the ASCA Galactic Plane Survey

Shigeo YAMAUCHI

*Faculty of Humanities and Social Sciences, Iwate University, 3-18-34 Ueda, Morioka, Iwate 020-8550
yamauchi@iwate-u.ac.jp*

Masaru UENO

Department of Physics, Faculty of Science, Tokyo Institute of Technology, 2-12-1 Oo-okayama, Meguro-ku, Tokyo 152-8551

Katsuji KOYAMA

*Department of Physics, Graduate School of Science, Kyoto University, Sakyo-ku, Kyoto 606-8502
and*

Aya BAMBA

*Institute of Space and Astronautical Science (ISAS), Japan Aerospace Exploration Agency (JAXA), 3-1-1 Yoshinodai,
Sagamihara, Kanagawa 229-8510*

(Received 2007 October 22; accepted 0 0)

Abstract

X-ray images and spectra of 5 cataloged supernova remnants (SNRs), G12.0–0.1, G346.6–0.2, G348.5+0.1, G348.7+0.3, and G355.6–0.0, observed in the ASCA galactic plane survey are presented. The sizes of X-ray emission from G12.0–0.1, G348.5+0.1, G348.7+0.3, and G355.6–0.0 are comparable to their radio structures, while that of G346.6–0.2 is smaller than the radio structure. The X-ray spectra of all of the SNRs were heavily absorbed by interstellar matter with $N_{\text{H}} > 10^{22} \text{ cm}^{-2}$. The spectrum of G355.6–0.0 exhibited emission lines, indicating that the X-ray emission has a thin thermal plasma origin, and was well represented by two-temperature thin thermal emission model. On the other hand, no clear emission line features were found in the spectra of the others and the spectra could be represented by either a thin thermal emission model or a power-law model.

Key words: ISM: individual (G12.0–0.1, G346.6–0.2, G348.5+0.1, G348.7+0.3, and G355.6–0.0) — ISM: supernova remnants — X-rays: ISM — X-rays: spectra

1. Introduction

Supernovae (SNe) and supernova remnants (SNRs) are very important objects, because they are main sites of heavy element production and of acceleration of high-energy particles in galaxies. X-ray observations of SNRs are useful for performing plasma diagnostics and for searching for synchrotron X-rays from high-energy electrons.

Many survey observations of galactic SNRs have been carried out mainly in the radio band and 265 SNRs have been cataloged so far (Green 2006). The Einstein Observatory detected X-rays from about 40 SNRs (e.g., Seward 1990), while the ROSAT all-sky survey detected X-rays from many SNRs including new SNRs (e.g., Pfeffermann et al. 1991; Pfeffermann & Aschenbach 1996; Voges et al. 1999). However, X-rays in the low energy band are absorbed by the interstellar medium, and hence soft X-ray observations can detect X-rays from only nearby SNRs on the galactic plane. On the other hand, although hard X-rays can observe SNRs even in the galactic plane, hard X-ray detectors without imaging capability could not find faint X-ray emission from SNRs on the galactic plane where there are many bright X-ray sources containing a compact object. The imaging capability in the hard X-ray band is essential to search for X-ray emis-

sion from SNRs located in the galactic disk.

ASCA was the first satellite carrying X-ray detectors with imaging capability in the 0.4–10.0 keV energy band (Tanaka et al. 1994). We performed survey observations on the galactic plane with ASCA. The ASCA galactic plane survey (AGPS) covered all the Galactic inner disk ($|l| < 45^\circ$ and $|b| < 0.4^\circ$) and the Galactic center region ($|l| < 2^\circ$ and $|b| < 2^\circ$) with successive pointing observations of about 10 ks exposure (Yamauchi et al. 2002). One of the major objectives of AGPS is to search for X-ray emission from cataloged radio SNRs and to investigate their properties. AGPS detected X-ray emissions from ~ 30 cataloged SNRs, including 15 SNRs undetected in the X-ray band before AGPS. (Yamauchi et al. 1998; Sugizaki et al. 2001; Sakano et al. 2002; Yamauchi et al. 2002). Results of several SNRs observed in AGPS have been reported by several authors (G352.7–0.1: Kinugasa et al. 1998; G359.0–0.9: Bamba et al. 2000; G359.1–0.5: Yokogawa et al. 2000; G359.1+0.9 and G1.9+0.3: Sakano et al. 2002; G344.7–0.1: Yamauchi et al. 2005). Furthermore, G15.9+0.2, G16.7+0.1, G338.3–0.0, and G349.7+0.2 have been observed with ASCA, Chandra, and XMM-Newton after the X-ray detection in AGPS, and the results have been reported (G15.9+0.2: Reynolds et al. 2006; G16.7+0.1: Helfand et al. 2003; G338.3–0.0: Funk et al. 2007; G349.7+0.2: Slane et al. 2002; Lazendic et al.

Table 1. The properties of SNRs.

Name	Position ^a (RA, Dec) _{J2000}	Size ^a (arcmin)	Type ^{a,b}	$F_{1\text{GHz}}^{a,c}$ (Jy)	$\Gamma_{\text{Radio}}^{a,d}$	F_{TeV}^e (erg s ⁻¹ cm ⁻²)	Γ_{TeV}^f
G12.0–0.1	(18 ^h 12 ^m 11 ^s , –18°37′)	7?	?	3.5	0.7	—	—
G346.6–0.2	(17 ^h 10 ^m 19 ^s , –40°11′)	8	S	8?	0.5?	—	—
G348.5+0.1	(17 ^h 14 ^m 06 ^s , –38°32′)	15	S	72	0.3	2.3×10 ⁻¹²	2.30
G348.7+0.3	(17 ^h 13 ^m 55 ^s , –38°11′)	17?	S	26	0.3	1.2×10 ⁻¹²	2.65
G355.6–0.0	(17 ^h 35 ^m 16 ^s , –32°38′)	8×6	S	3?	?	—	—

^a Green (2006) and references therein.^b S: shell-type and C: composite-type.^c Radio flux at 1 GHz.^d Spectral index in the radio band.^e Unabsorbed energy flux in the 1–10 TeV energy band (Aharonian et al. 2008a, 2008b).^f Power-law index of the TeV γ -ray spectrum (Aharonian et al. 2008a, 2008b).**Table 2.** The observation logs.

Name	Observation date	Pointing position (RA, Dec) _{J2000}	$\Delta\theta^a$ (arcmin)	Exposure time (ks)
G12.0–0.1	1996 April 9	(18 ^h 11 ^m 53.9 ^s , –18°32′03.1″)	6.4	6.3
G346.6–0.2	1996 September 3	(17 ^h 09 ^m 34.1 ^s , –39°59′35.9″)	14.3	8.2
G348.5+0.1	1996 September 12	(17 ^h 15 ^m 38.1 ^s , –38°22′37.2″)	20.3	7.8
G348.7+0.3	1996 September 12	(17 ^h 15 ^m 38.1 ^s , –38°22′37.2″)	23.3	7.8
G355.6–0.0	1996 March 16	(17 ^h 34 ^m 57.5 ^s , –32°34′54.5″)	5.0	9.8

^a Separation angle between the SNR position (see table 1) and the FOV center.

2005). In this paper, we report on results of other 5 SNRs, G12.0–0.1, G346.6–0.2, G348.5+0.1, G348.7+0.3, and G355.6–0.0, obtained from the AGPS data. The properties of the SNRs are listed in table 1.

2. Observations and Data Reduction

AGPS was performed in 1996–1999. ASCA carried two Solid-state Imaging Spectrometers (SIS0, SIS1) and two Gas Imaging Spectrometers (GIS2, GIS3) placed at the focal planes of four thin foil X-ray Telescopes (XRT). Each SIS camera, consisting of 4-CCD chips, was operated in 4-CCD mode or 2-CCD mode. In order to avoid telemetry overflow, the lower discriminator was set to be 0.7 keV, and hence the effective energy range of the SIS was 0.7–10 keV. On the other hand, the GIS was operated in PH mode with the 0.7–10 keV band. The two sets of the SIS covered 22′×22′, while the field of view (FOV) of the GIS was 50′ in diameter. Details of ASCA and the instruments are given in separate papers (ASCA satellite: Tanaka et al. 1994; XRT: Serlemitsos et al. 1995; SIS: Burke et al. 1991; GIS: Makishima et al. 1996; Ohashi et al. 1996).

The SIS data quality exhibited significant degradation due mainly to the particle irradiation (Dotani et al.

1995; Yamashita et al. 1997). The most serious problem for the present SNR observation is the increase of pixel-to-pixel fluctuation of the dark current (Residual Dark Distribution, RDD), which makes the energy resolution worse. Therefore, we concentrate on results using the GIS data.

We excluded the data obtained at the South Atlantic Anomaly, during the earth occultation, at the low elevation angle from the earth rim of < 5°, and in the high background regions at low geomagnetic cut off rigidities of < 8 GV. We also applied a rise-time discrimination technique to reject particle events. The observation logs are listed in table 2.

3. Analysis and Results

The survey area contained ~ 60 SNRs cataloged before AGPS (Green 2006) and AGPS detected X-ray emission at the positions of ~ 30 SNRs, including 15 SNRs undetected in the X-ray band before AGPS. Here, we report on the X-ray properties of 5 SNRs of which X-ray properties have not been reported. The X-ray images in the 0.7–10.0 keV energy band for GIS2 and GIS 3 were made and the data obtained with GIS2 and GIS3 were combined. The X-

Table 3. The best-fit parameters of spectral analysis^a.

Name	Model ^b	kT / α^c	N_H^d	χ^2 (d.o.f.)	F_{obs}^e	F_{unabs}^f
G12.0–0.1	1T	1.6 (>0.7)	6.5 (1.0–13.8)	5.24 (12)	0.79	6.4
	PL	3.1 (1.2–6.3)	5.9 (1.4–14.7)	4.31 (12)	0.91	8.7
G346.6–0.2	1T	1.6 (0.4–4.7)	2.0 (0.4–5.5)	11.00 (18)	1.3	5.6
	PL	3.7 (>1.7)	2.6 (0.4–10.8)	12.06 (18)	1.3	18
G348.5+0.1	1T	2.2 (1.8–3.2)	2.0 (1.4–2.5)	34.98 (40)	6.6	18
	1Tv ^g	2.8 (2.1–4.4)	1.7 (1.2–2.3)	26.68 (39)	6.9	15
	PL	3.0 (2.4–3.6)	2.4 (1.8–3.2)	32.84 (40)	6.7	36
G348.7+0.3 ^h	1T	1.6 (0.9–2.6)	2.7 (1.4–5.1)	18.49 (17)	2.5	12
	PL	4.1 (2.8–6.1)	4.0 (2.0–7.3)	17.76 (17)	2.5	82
G355.6–0.0	1T	1.0 (0.6–1.5)	4.0 (2.8–5.4)	27.55 (27)	0.81	17
	2T	0.7 (0.3–1.0)	4.4 (3.2–6.6)	21.03 (25)	0.58	40
		7.5 (> 1.7)	4.4 ⁱ	—	0.48	0.94
	PL	4.5 (3.2–6.2)	4.4 (2.7–6.7)	32.95 (27)	0.90	50

^a Values in parentheses show 90% confidence intervals.

^b PL: power-law model, 1T: single-temperature MEKAL model with the Solar abundances, 1Tv: single-temperature MEKAL model with variable abundances, 2T: 2-temperature MEKAL model with the Solar abundances.

^c Temperature (keV)/photon index.

^d Hydrogen column density in unit of 10^{22} cm^{-2} .

^e Observed X-ray flux in the 0.5–10 keV energy band calculated using the best-fit parameters. The unit is $10^{-12} \text{ erg s}^{-1} \text{ cm}^{-2}$.

^f N_H -corrected X-ray flux in the 0.5–10 keV energy band calculated using the best-fit parameters. The unit is $10^{-12} \text{ erg s}^{-1} \text{ cm}^{-2}$.

^g The Si abundance was set to be free; $\text{Si}=4.3^{+6.1}_{-2.3}$ Solar.

^h ASCA observed only the southern part of the SNR because the SNR was located near to the edge of the GIS FOV.

ⁱ The same N_H value as that for the low-temperature component was assumed.

ray spectrum was extracted from the region including the SNR. The background spectrum was extracted from the source free region in the same FOV. In order to maximize photon statistics, the data obtained with GIS2 and GIS3 were combined.

Several studies reported that there were some differences in the energy scales between the SIS and the GIS and that a gain adjustment of 2–3 % was required for the GIS analysis (Miyata 1996; Yamauchi et al. 1999; Slane et al. 2002; Yamauchi et al. 2005). However, since the photon statistics were limited due to short exposure time and low source flux, the precise gain adjustment was impossible for the present analysis. Taking account of these facts, we used two simple models for a spectral analysis; a thin thermal emission model from a plasma in the collisional ionization equilibrium (MEKAL model; Mewe et al. 1985; Liedahl et al. 1995; Mewe et al. 1995) and a power-law model, and did not apply a more detailed model such as a non-ionization equilibrium model. The abundance table were taken from Anders and Grevesse (1989), while the cross sections of photoelectric absorption were taken from Morrison and McCammon (1983). We, at first, assumed the abundances to be solar, but in some cases we set the metal abundances to be free. Results of the spectral analysis are summarized in table 3. X-ray properties for each SNR are described in the following section.

3.1. G12.0–0.1

X-ray detection of G12.0–0.1 in AGPS and results of a power-law model fit were reported by Sugizaki et al. (2001). The radio structure shows an incomplete shell, where only the eastern half is visible (figure 1, e.g., Condon et al. 1998). The bright source at the western part in the radio band image is a thermal radio source containing an ultracompact HII region (Downes et al. 1980; Becker et al. 1994). The X-ray image (the gray scale in figure 1) displayed weak X-ray emission. However, no clear X-ray peak was seen at the position of the western bright radio source.

The X-ray spectrum was extracted from a $4.5'$ radius circle including the arc-like structure in the radio band. The background spectrum was extracted from an annular region between $9'$ and $4.5'$ radius, but X-ray photons from the $3'$ radius circle around AX J181213–1842 (Sugizaki et al. 2001) and two local peaks at the north of G12.0–0.1, not listed in Sugizaki et al. (2001), were excluded. The X-ray counts from the source region in the 0.7–10 keV energy band were 568 (GIS2+3), while the background counts in the same region size and in the same energy band were estimated to be 446 (GIS2+3). Since the photon statistics were limited, the X-ray spectrum was well explained by either a MEKAL model or a power-law model. The X-ray spectrum and the best-fit power-law model are shown

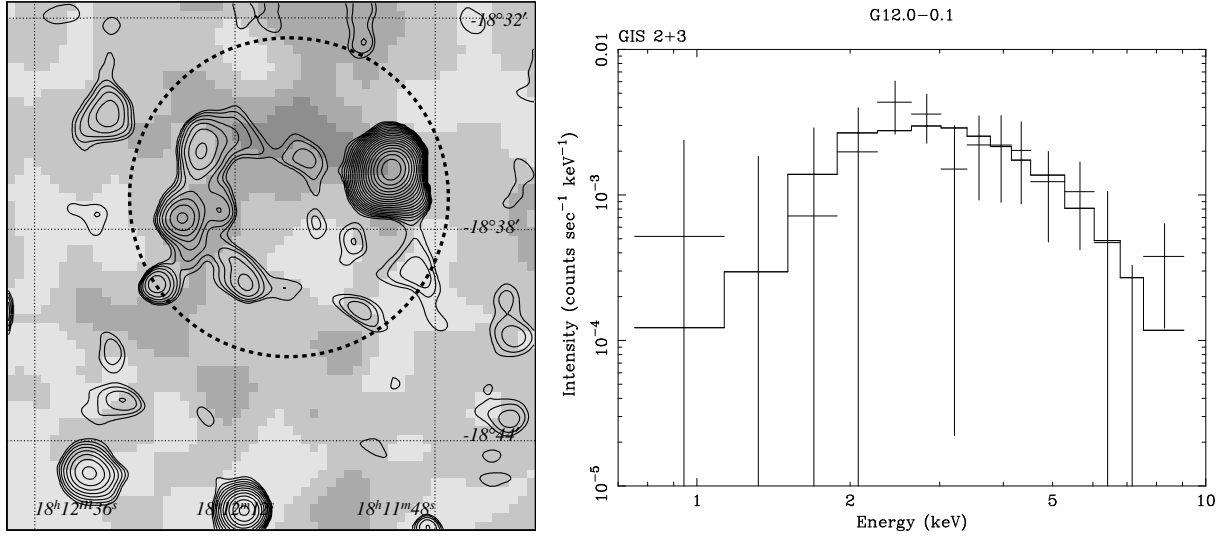


Fig. 1. Left: GIS 2+3 image of G12.0-0.1 obtained in the 0.7–10.0 keV energy band (gray scale). The X-ray image was smoothed with a Gaussian distribution of $\sigma = 30''$. The coordinates are J2000. The intensity level are linearly spaced by $0.2 \text{ counts pixel}^{-1}$. The contour shows a radio intensity map at 1.4 GHz using the NRAO VLA Sky Survey (NVSS) (Condon et al. 1998). The dotted line shows the region from which the X-ray spectrum was extracted. Right: GIS spectrum of G12.0-0.1 (the crosses) and the best-fit power-law model (the histogram).

in figure 1. The spectral parameters obtained from the power-law model fit were consistent with those in Sugizaki et al. (2001) within errors. The differences in the best-fit spectral parameters between Sugizaki et al. (2001) and our analysis would be due to the differences in the source region: in Sugizaki et al. (2001), the spectrum was extracted within $3'$ from the source center, while in this analysis, the spectrum was extracted from the $4.5'$ radius circle including the radio shell.

3.2. G346.6-0.2

The radio and X-ray images are shown in figure 2. G346.6-0.2 was located near to the edge of the GIS FOV. The radio shell with a $\sim 8'$ diameter was found (e.g., Whiteoak, Green 1996), while an X-ray image shows an existence of a weak emission in the radio shell.

The X-ray spectrum was extracted from a $5'$ radius circle, while the background spectrum was extracted from an annular region between $7'$ and $5'$ radius. The X-ray counts from the source region in the 0.7–10 keV energy band were 1258 (GIS2+3), while the background counts in the same region size and in the same energy band were estimated to be 1059 (GIS2+3). The spectrum was explained by either a MEKAL model with a temperature of 1.6 keV or a single power-law model with a photon index of 3.7, although the errors are large due to the limited photon statistics. The best-fit power-law model is shown in figure 2.

3.3. G348.5+0.1

The field centered on $(l, b) = (348^\circ 7, 0^\circ 0)$ includes 3 radio SNRs, G348.5-0.0, G348.5+0.1, and G348.7+0.3. X-ray emissions from G348.5+0.1 and G348.7+0.3 were clearly found, but that of G348.5-0.0 was not clearly

seen due to the stray light from a nearby bright source. This data were excluded in the analysis by Sugizaki et al. (2001).

Figure 3 shows an X-ray image around G348.5+0.1. G348.5+0.1 was located near to the edge of the GIS FOV. An extended emission with a diameter of $\sim 6'$ was clearly found at the position of G348.5+0.1. The extended X-ray emission well coincides with the bright northern part of the radio structure (e.g., Whiteoak, Green 1996).

The X-ray spectrum was extracted from a $5'$ radius circle. Since the stray light from the nearby bright source was found near G348.5+0.1, the background spectrum for G348.5+0.1 was extracted from the source free region with a radius of $7.5'$ at the same distance from the Galactic plane and from the FOV center. The X-ray counts from the source region in the 0.7–10 keV energy band were 1483 (GIS2+3), while the background counts in the same region size and in the same energy band were estimated to be 593 (GIS2+3). Due to the poor statistics, the spectrum was well represented by either a thin thermal emission model with a temperature of 2.2 keV and Solar abundances or a power-law model with a photon index of 3. Even if we applied a MEKAL model with the Solar abundances, we found positive residuals at the Si-line band, which may show that a thin thermal emission is preferable. We applied a MEKAL model with freeing the Si abundance to the spectrum. The best-fit MEKAL model with freeing the Si abundance (model 1Tv in table 3) is shown in figure 3.

3.4. G348.7+0.3

We found a source near to the edge of the GIS FOV (figure 4). Compared with a radio continuum image (e.g., Whiteoak, Green 1996), we found that the X-ray source

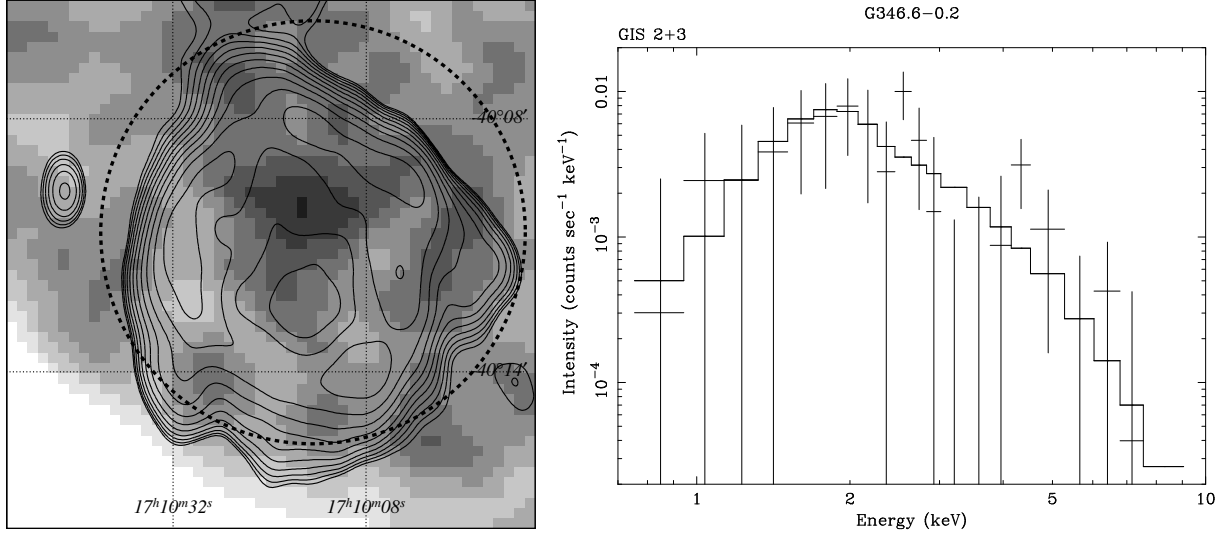


Fig. 2. Left: GIS 2+3 image of G346.6–0.2 obtained in the 0.7–10.0 keV energy band (gray scale). The intensity level are linearly spaced by 0.2 counts pixel^{−1}. The contour shows a radio intensity map at 843 MHz using the Molonglo Observatory Synthesis Telescope (MOST) (Whiteoak, Green 1996). The dotted line shows the region from which the X-ray spectrum was extracted. Right: GIS spectrum of G346.6–0.2 (the crosses) and the best-fit power-law model (the histogram).

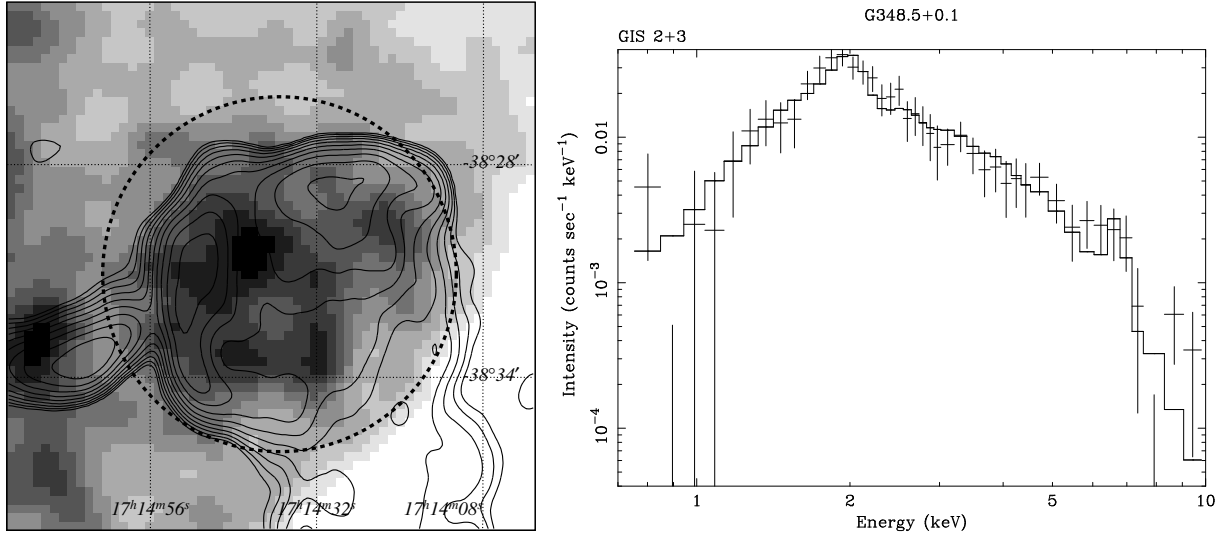


Fig. 3. Left: GIS 2+3 image of G348.5+0.1 obtained in the 0.7–10.0 keV energy band (gray scale). The intensity level are linearly spaced by 0.2 counts pixel^{−1}. The contour shows a radio intensity map by MOST. The dotted line shows the region from which the X-ray spectrum was extracted. Right: GIS spectrum of G348.5+0.1 (the crosses) and the best-fit MEKAL model with freeing the Si abundance (the histogram).

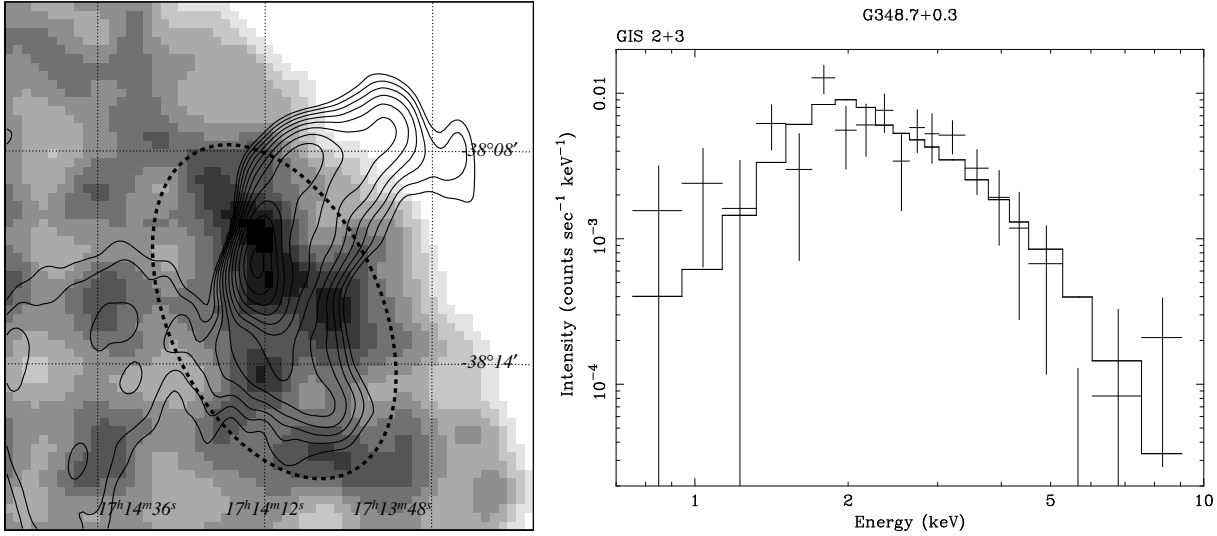


Fig. 4. Left: GIS 2+3 image of G348.7+0.3 obtained in the 0.7–10.0 keV energy band (gray scale). The intensity level are linearly spaced by 0.2 counts pixel⁻¹. The contour shows a radio intensity map by MOST. The dotted line shows the region from which the X-ray spectrum was extracted. Right: GIS spectrum of G348.7+0.3 (the crosses) and the best-fit power-law model (the histogram).

coincides with a southern part of G348.7+0.3.

The X-ray spectrum was extracted from an elliptical region with a major axis of 10' and a minor axis of 6'. The background spectrum was extracted from an elliptical region surrounding G348.7+0.3 with a major axis of 20' and a minor axis of 11', but excluded the source region. The X-ray counts from the source region in the 0.7–10 keV energy band were 641 (GIS2+3), while the background counts in the same region size and in the same energy band were estimated to be 379 (GIS2+3). Both a MEKAL model ($kT \sim 1.6$ keV) and a power-law model ($\alpha \sim 4$) can explain the X-ray spectrum. The precise calibration for the outer region of the GIS FOV was not established. Since the SNR was located near to the edge of the GIS FOV, the systematic errors of the parameters were large.

3.5. G355.6–0.0

X-ray detection of G355.6–0.0 in AGPS and results of a power-law model fit were reported by Sugizaki et al. (2001). A bright X-ray source in the image (figure 5) is a young open cluster NGC 6383. G355.6–0.0 was located at the east of NGC 6383. An extended X-ray emission was found at the position of G355.6–0.0. The size was comparable to that of the radio band ($\sim 8' \times 6'$, e.g., Condon et al. 1998)

The X-ray spectrum was extracted from an elliptical region with a major axis of 8' and a minor axis of 6'. The background spectrum was extracted from an annular region between 10' and 5' radius, but the contribution from NGC 6383 were excluded. The X-ray counts from the source region in the 0.7–10 keV energy band were 775 (GIS2+3), while the background counts in the same region size and in the same energy band were estimated to be 423 (GIS2+3). The results of the spectral fit are listed in table 3. Taking account of the errors, we found that the power-law model fit are consistent with those in Sugizaki et al.

(2001). The X-ray spectrum of G355.6–0.0 exhibited an emission line from Si (figure 5), which suggested that it is thermal plasma emission. Although the photon statistics are limited, the X-ray spectrum inferred the presence of a Fe K-line emission. When a single-temperature MEKAL model was applied, systematic residuals were found above 5 keV energy band. If we let metal abundance be free, high Si and Fe abundances were required and positive residuals in the high energy band remained. This indicates the presence of the additional high-temperature component. Thus, we applied a two-temperature MEKAL model and obtained an acceptable fit with temperatures of $0.7^{+0.3}_{-0.4}$ keV and 7.5 (>1.7) keV and Solar abundances.

4. Discussion and Conclusions

AGPS covered all the Galactic inner disk ($|l| < 45^\circ$ and $|b| < 0.4^\circ$) and the Galactic center region ($|l| < 2^\circ$ and $|b| < 2^\circ$) and detected X-ray emissions from many X-ray sources embedded in the Galactic plane, which provided us with new information on their X-ray emission. AGPS detected X-rays from ~ 30 cataloged SNRs, including 15 SNRs undetected in the X-ray band before AGPS. We presented X-ray images and X-ray spectra of 5 SNRs among them, G12.0–0.1, G346.6–0.2, G348.5+0.1, G348.7+0.3, and G355.6–0.0.

The sizes of X-ray emissions from G12.0–0.1, G348.5+0.1, G348.7+0.3, and G355.6–0.0 are comparable to their radio structures, while that of G346.6–0.2 is smaller than the radio structure. All of the X-ray spectra were heavily absorbed by interstellar matter ($N_H > 10^{22}$ cm⁻²) and their X-ray fluxes in the 0.5–10.0 keV energy band were in the range of $\sim 10^{-12}$ – 10^{-11} erg s⁻¹ cm⁻². The Galactic plane contains a large amount of absorbing matters and many bright X-ray binary sources. The large N_H value and low flux of the SNRs (probably due to long

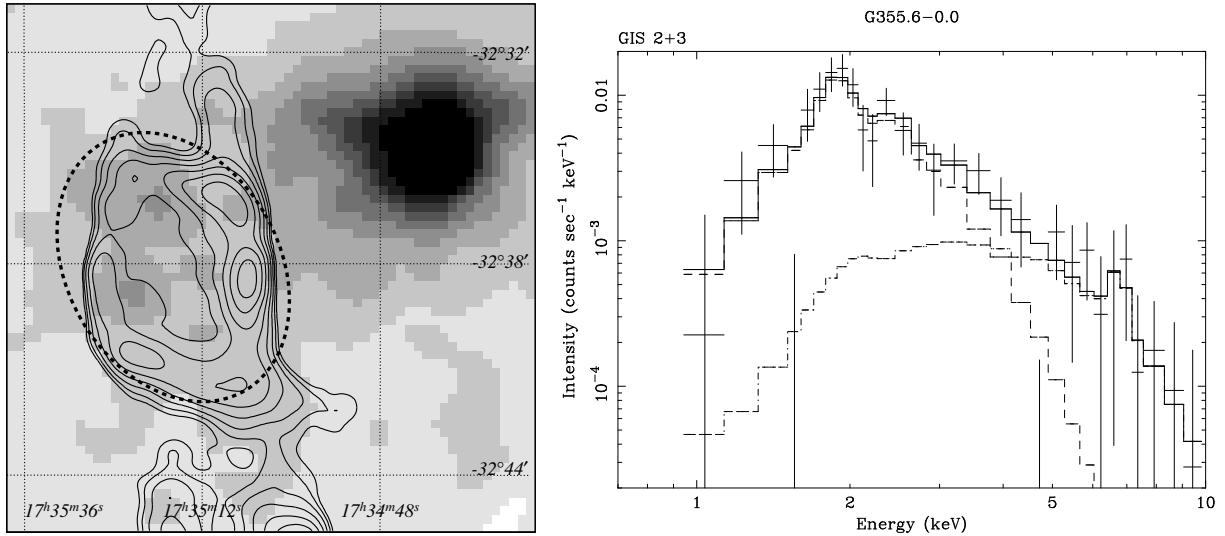


Fig. 5. Left: GIS 2+3 image of G355.6–0.0 obtained in the 0.7–10.0 keV energy band (gray scale). The bright X-ray source in the upper right is a young open cluster NGC 6383. The intensity level are linearly spaced by 0.4 counts pixel^{−1}. The contour shows a radio intensity map by NVSS. The dotted line shows the region from which the X-ray spectrum was extracted. Right: GIS spectrum of G355.6–0.0 (the crosses) and the best-fit 2 MEKAL model (the histogram). The each component is shown by the dashed line and the dash-dotted line.

distances to the SNRs) are the reason why their X-ray emissions could not be detected before AGPS.

Recently, Aharonian et al. (2008a, 2008b) reported detection of TeV γ -ray emission from G348.5+0.1 and G348.7+0.3 with High Energy Stereoscopic System (H.E.S.S.) (HESS J1714–385 and HESS J1713–381, respectively) and results of follow up X-ray observations of the SNRs with Chandra and XMM-Newton. They resolved the X-ray emission detected in AGPS into an extended thermal emission and several point-like sources and discussed the nature of the X-ray and γ -ray sources in detail. The X-ray spectra of G348.5+0.1 and G348.7+0.3 obtained in AGPS contain X-ray emissions from the extended source and the point-like sources. We confirmed that the ASCA spectra of G348.5+0.1 and G348.7+0.3 were well represented by a model consisting of X-ray emissions from the extended and point-like sources reported in Aharonian et al. (2008a, 2008b).

Here, we briefly discuss on the X-ray emission from the other three SNRs, G12.0–0.1, G346.6–0.2, and G355.6–0.0. The spectrum of G355.6–0.0 exhibited a Si-K line (and possibly a Fe-K line), which indicates that the X-ray emission has a thin thermal plasma origin. On the other hand, no clear emission line features were found in the spectra of the others and their spectra could be represented by either a thin thermal emission model or a power-law model.

Although errors are large, the temperatures of G12.0–0.1, G346.6–0.2, and G355.6–0.0 derived from the MEKAL model fits (1–2 keV) are consistent with those of SNRs. Assuming that the SNRs are in the Sedov phase (Sedov 1959), we examined a case of a shell-like SNR with thin thermal X-ray emission. The size of the SNR is derived from the radio and X-ray images, while

the plasma temperature (kT_X) and the emission integral ($EI = \int n_H n_e dV$, n_H and n_e are the hydrogen and electron densities, respectively, V is the volume of the X-ray emitting region) are taken from the MEKAL model fit. The distances to the SNRs were calculated from the best-fit N_H values with assumption of the mean density of 1 Hcm^{−3}. For G355.6–0.0, we assumed the low-temperature component is X-ray emission from the shell region. Assuming the temperature of the SNR shell (kT_S) of $kT_S = 0.775 kT_X$, the filling factor of 0.25, and $n_e = 1.2 n_H$, the explosion energies for G12.0–0.1, G346.6–0.2, and G355.6–0.0 were calculated to be ~ 1 , ~ 0.05 , and ~ 0.5 in units of 10^{51} erg, respectively. Although the uncertainties of the physical parameters derived from the spectral fits are large, the case of G346.6–0.2 seems to be much smaller than the canonical supernova explosion energy ($=10^{51}$ erg).

Next, we examined two cases of nonthermal X-ray emission from the SNR for G12.0–0.1 and G346.6–0.2, a SN 1006-like case and a pulsar wind nebula (PWN) case. In the case of SN 1006-like SNRs, high energy electrons accelerated in the SNR shells emit synchrotron X-rays and lose their energy. The observed flux densities at 10^{18} Hz were $\sim 9 \times 10^{-8}$ Jy and $\sim 7 \times 10^{-8}$ Jy for G12.0–0.1 and G346.6–0.2, respectively, which are smaller than the values extrapolated from the radio band with the parameters in table 1 (Green 2006), $\sim (1-2) \times 10^{-6}$ Jy and $\sim 3 \times 10^{-4}$ Jy for G12.0–0.1 and G346.6–0.2, respectively. Furthermore, although the errors are large, the spectral indices in the X-ray band obtained from the power-law model fit were steeper than those in the radio band. These suggest that there is a break frequency between the radio and the X-ray bands. Therefore, the nonthermal X-rays from the SNR shells like SN 1006, may be possible. The X-ray morphology of G346.6–0.2 seems to show a weak

peak in the radio structure. Although a pulsar has not been discovered for G346.6–0.2, a PWN scenario can not be excluded.

Unfortunately, detailed properties of the SNRs are still unknown because the photon statistics in the AGPS data were limited. In order to understand the physical process in the SNRs and their nature, spatially resolved X-ray spectra with good photon statistics with Chandra, XMM-Newton, and Suzaku are required.

We would like to express our thanks to all of the ASCA team. This work is supported in part by the Grant-in-Aid for Scientific Research from the Japan Society for the Promotion of Science (JSPS) (Nos. 15540225 and 18540228; S.Y.). M. U. and A. B. are supported by Research Fellowships for Young Scientists of JSPS.

References

- Aharonian, F., et al. 2008a, submitted to A&A, arXiv 0803.0682
- Aharonian, F., et al. 2008b, submitted to A&A, arXiv 0803.0702
- Anders, E., & Grevesse, N. 1989, *Geochim. Cosmochim. Acta*, 53, 197
- Bamba, A., Yokogawa, J., Sakano, M., & Koyama, K., 2000, *PASJ*, 52, 259
- Becker, R. H., White, R. L., Helfand, D. J., & Zoonematkermani, S. 1994, *ApJS*, 91, 347
- Burke B. E., Mountain R. W., Harrison D. C., Bautz M. W., Doty J. P., Ricker G. R., & Daniels P. J. 1991, *IEEE Trans.*, ED-38, 1069
- Condon, J. J., Cotton, W. D., Greisen, E. W., Yin, Q. F., Perley, R. A., Taylor, G. B., & Broderick, J. J. 1998, *AJ*, 115, 1693
- Dotani, T., Yamashita, A., Rasmussen, A., & the SIS team 1995, *ASCA News*, 3, 25
- Downes, D., Wilson, T. L., Bieging, J., & Wink, J. 1980, *A&AS*, 40, 379
- Funk, S., Hilton, J. A., Pühlhofer, G., Aharonian, F. A., Hofmann, W., Reimer, O., & Wagner, S. 2007, *ApJ*, 662, 517
- Green, D. A. 2006, *A Catalog of Galactic Supernova Remnants* (2006 April version), (Cambridge, UK, Mullard Radio Astronomy Observatory) ¹
- Kinugasa, K., Torii, K., Tsunemi, H., Yamauchi, S., Koyama, K., & Dotani, T. 1998, *PASJ*, 50, 249
- Helfand, D. J., Agüeros, M. A., & Gotthelf, E. V. 2003, *ApJ*, 592, 941
- Lazendic, J. S., Slane, P. O., Hughes, J. P., Chen, Y., & Dame, T. M. 2005, *ApJ*, 618, 733
- Liedahl, D. A., Osterheld, A. L., & Goldstein, W. H. 1995, *ApJ*, 438, L115
- Makishima, K., et al. 1996, *PASJ*, 48, 171
- Mewe, R., Gronesechild, E. H. B. M., & van den Oord, G. H. J. 1985, *A&AS*, 62, 197
- Mewe, R., Kaastra, J. S., & Liedahl, D. A. 1995, *Legacy*, 6, 16
- Miyata, E. 1996, Ph. D. Thesis, Osaka University
- Morrison, R., & McCammon, D. 1983, *ApJ*, 270, 119
- Ohashi, T., et al. 1996, *PASJ*, 48, 157
- Pfeffermann, E., Aschenbach, B., & Predehl, P. 1991, *A&A*, 246, L28
- Pfeffermann, E., & Aschenbach, B. 1996, *Röntgenstrahlung from the Universe* (MPE report 263), 267
- Reynolds, S. P., Borkowski, K. J., Hwang, U., Harrus, I., Petre, R., & Dubner, G. 2006, *ApJ*, 652, 45
- Sakano, M., Koyama, K., Murakami, H., Maeda, Y., & Yamauchi, S. 2002, *ApJS*, 138, 19
- Sedov, L. I. 1959, *Similarity and Dimensional Methods in Mechanics* (New York: Academic)
- Serlemitsos, P. J., et al. 1995, *PASJ*, 47, 105
- Seward, F. D. 1990, *ApJS*, 73, 781
- Slane, P., Chen, Y., Lazendic, J. S., & Hughes, J. P. 2002, *ApJ*, 580, 904
- Sugizaki, M., Mitsuda, K., Kaneda, H., Matsuzaki, K., Yamauchi, S., & Koyama, K. *ApJS*, 2001, 134, 77
- Tanaka Y., Inoue H., & Holt S. S. 1994, *PASJ* 46, L37 2000, *PASJ*, 52, 887
- Voges, W., et al. 1999, *A&A*, 349, 389
- Whiteoak, J. B. Z., & Green A. J. 1996, *A&AS*, 118, 329
- Yamashita, A., et al. 1997, *IEEE Trans. Nuclear Science*, 44, 847
- Yamauchi, S., Koyama, K., Kinugasa, K., Torii, K., Nishiuchi, M., Kosuga, T., Kamata, Y., & ASCA Galactic Plane Survey team 1998, *Astron. Nachr.*, 319, 111
- Yamauchi, S., Koyama, K., Tomida, H., Yokogawa, J., & Tamura, K. 1999, *PASJ*, 51, 13
- Yamauchi, S., et al. 2002, *Proc. of the IAU 8th Asian-Pacific Regional Meeting Vol.II (ASJ)*, p81
- Yamauchi, S., Ueno, M., Koyama, K., & Bamba, A. 2005, *PASJ*, 57, 459
- Yokogawa, J., Sakano, M., Koyama, K., & Yamauchi, S. 2000, *Adv. Space Res.*, 25, 571

¹ <http://www.mrao.cam.ac.uk/surveys/snrns/>